Article

Diffusion Characteristics of Airflow and CO in the Dead-End Tunnel with Different Ventilation Parameters after Tunneling Blasting

Jinmiao Wang, Yan Xue, Jun Xiao, and Dongping Shi*

ACCESS | Metrics & More | Article Recommendations

ABSTRACT: After tunnel blasting, a large amount of CO will be produced and accumulated in the dead-end tunnel. If the ventilation discharge is not proper and the entry time into the dead-end tunnel is not appropriate, then it can cause workers to suffer from poisoning, hypoxia, and suffocation. Therefore, to understand the airflow and diffusion characteristics of CO in the dead-end tunnel after excavation and improve the working environment quality of the heading excavation tunnel, this paper uses numerical simulation and on-site verification to study the influence of different ventilation parameters on the airflow and CO diffusion characteristics in the dead-end tunnel after excavation and blasting. The research results show that the higher the air velocity of the duct, the smaller the distance between the duct and the working face, and the higher the hanging height of the duct, the easier it is for CO to be discharged from the dead-end tunnel. The larger the distance between the duct and the side wall, the more vortices there are in the dead-end tunnel and the more difficult it is to discharge CO from the tunnel. This study provides theoretical guidance for the research of the migration law of CO after tunnel blasting and has important value for ensuring a safe working environment and clean production in tunnel excavation.
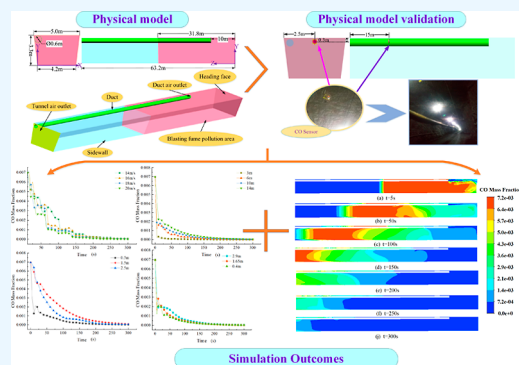
1. INTRODUCTION

The ventilation and working environment problems of the dead-end tunnel have been troubling ventilation engineers and mining professionals during underground mining.[1,2] The dead-end tunnel is an important part of underground mining, but with only one exit, it is difficult to form a continuous airflow in the roadway.[3,4] Toxic and harmful gases and dust are prone to accumulate and difficult to discharge in the dead-end tunnel, and the concentration of toxic and harmful gases and dust in the roadway cannot reach the allowable concentration stipulated by the country, which seriously threatens life, health, and safety of underground workers.[5−7]

So far, many scholars have conducted extensive research on the influence of ventilation parameters on airflow distribution, toxic and harmful gases, and dust in the dead-end tunnel.[8−11] For example, Wang investigated the changes of gas and dust near the driving face when the distance between the duct and the face was different, and selected the optimal distance for duct installation.[12] Lu analyzed the effects of different ventilation parameters on the airflow field and gas distribution and concluded that the duct had a better effect on eliminating gas when the distance between the duct and the roadway floor was 1.75 m.[13] Zhang studied the distribution of blasting smoke in the roadway when the duct was at different heights and distances from the working face and obtained the optimal layout of the duct.[14] Wei discussed and analyzed the effects of duct hanging height, duct diameter, and distance from the

working face on the distribution of dust in the roadway and selected the ventilation parameters with the best dust reduction effect.[15] Wencai analyzed the changes in the airflow field in the roadway when the distance and hanging height of the duct were different from the working face and obtained the optimal ventilation parameters in the roadway.[3] Xie analyzed the distribution of air velocity and dust in the roadway when the duct was arranged in different positions and obtained the best layout of the duct.[16] Wei, respectively, explored the distribution of airflow and dust in the roadway when the duct hanging height and distance from the working face were different and found that the duct hanging height had the greatest influence on the distribution of eddy currents.[17] Huang analyzed the influence of the distance between the duct and the working face on the distribution of CO in the roadway and found that the dispersibility coefficient of CO in the roadway was proportional to the distance between the duct and the working face.[18]

The previous studies mainly focused on analyzing the effects of different ventilation parameters on the airflow, gas, and dust concentration evolution in the roadway.[11,19−21] However, after tunneling and blasting, a large amount of toxic and harmful gas, mainly CO, is generated in the dead-end tunnel. If the fresh air flow in the dead-end tunnel is insufficient or the ventilation time is not timely, it can easily cause mine explosion, smoke and dust poisoning, and personnel casualties.[22−27] Among the toxic and harmful gases, NO_X and CO are the most hazardous. NO_X is unstable and soluble in water; its concentration significantly decreases after spray dust removal. In contrast, CO is more stable and remains a primary cause of poisoning among tunnel personnel. Therefore, this paper assumes that postblasting pollution in the dead-end tunnel consists only of CO. The study focuses on the diffusion characteristics of airflow and the spatiotemporal evolution of CO concentration under different ventilation parameters in the dead-end tunnel.

Apart from the introduction, this article is organized as follows: Section 2 establishes a dead-end roadway model, divides it into a hexahedral grid, and performs an independence test to select the grid size that meets the accuracy requirements. Section 3 explores the influence of air velocity in the air duct, distance from the working face, distance from the roadway side, and suspension height on the airflow and CO distribution in the dead-end roadway, determining the optimal air velocity and layout position of the air duct in the roadway. Section 4 summarizes and generalizes the impact of four different ventilation parameters on the airflow field and the CO concentration in the dead-end roadway.

2. MATHEMATICAL AND PHYSICAL MODELS

In this study, the simulation of airflow and CO diffusion characteristics in a dead-end tunnel is carried out using finite element software (ANSYS FLUENT).[28] First, a mathematical model that reflects the actual situation needs to be selected.[29] Then, a physical model is established using DesignModeler, followed by the use of ICEM CFD to partition the hexahedral mesh, conduct a grid independence check to determine the various parameters and boundary conditions in the FLUENT numerical simulation process, and finally validate the model.

2.1. Mathematical Model. After blasting in a dead-end tunnel, the movement of CO in the tunnel space is a single-phase multicomponent diffusion process that conforms to the three laws of conservation of momentum, energy, and mass, as well as turbulent motion equations.[30]

2.1.1. Continuity Equation. Any fluid motion problem must satisfy the law of conservation of mass, and the corresponding equation is also called the continuity equation.[31] The expression is as follows[32]

$$\frac{\partial \rho}{\partial t} + \frac{\partial(\rho u)}{\partial x} + \frac{\partial(\rho v)}{\partial y} + \frac{\partial(\rho w)}{\partial z} = 0 \tag{1}$$

where ρ is the gas density, kg/m³; t is the time, s; and u, v, and w are velocity components in the x, y, and z directions, respectively, m/s.

2.1.2. Momentum Equation. The momentum conservation equation, also known as the Navier−Stokes equation, is expressed as follows

$$\frac{\partial(\rho u)}{\rho t} + \frac{\partial(\rho u_i u_j)}{\partial x_i} = -\frac{\partial p}{\partial x_i} + \frac{\partial \tau_{ij}}{\partial x_j} + \rho g_i + F_i \tag{2}$$

where P is the static pressure,[33] Pa; τ_{ij} is the Reynolds stress tensor; g_i and F_i, respectively, denote the volumetric gravitational force and external force in the i-direction.

2.1.3. Energy Equation. The law of energy conservation is a fundamental law that must be satisfied by any flow system that involves heat exchange. The specific formula is as follows

$$\frac{\partial(\rho T)}{\partial t} + \text{div}(\rho u T) = \text{div}\left(\frac{k}{C_p}\text{grad } T\right) + S_T \tag{3}$$

where T is the temperature, K; k is the fluid heat transfer coefficient; C_p is the specific heat capacity, J/(kg·K); S_T are the internal heat sources of the fluid and the portion of mechanical energy converted into thermal energy due to viscous effects.[34]

2.1.4. Realizable k-Epsilon Turbulence Model. The K-equation of the realizable $k−\varepsilon$ model is expressed as follows

$$\frac{\partial}{\partial t}(\rho k) + \frac{\partial}{\partial x_i}(\rho u_i k)$$
$$= \frac{\partial}{\partial x_i}\left[\left(\mu + \frac{\mu_t}{\sigma_k}\right)\frac{\partial k}{\partial x_i}\right] + G_k + G_b - \rho\varepsilon - Y_M + S_k \tag{4}$$

where $\sigma_k = 1.0$; G_k is the turbulence kinetic energy generated due to the mean velocity gradient; G_b is the turbulence kinetic energy generated due to buoyancy effects; Y_M is the contribution of turbulent expansion due to compressibility effects to the total dissipation rate; μ is the dynamic viscosity coefficient, Pa·s; $\rho\varepsilon$ is the dissipation term; μ_t is the turbulent viscosity ratio, $\mu_t = \rho C_\mu k^2 / \varepsilon$

In the realizable $k−\varepsilon$ model, to ensure constraints on the positive stress, C_μ is no longer considered a constant but is instead related to the strain rate. The calculation formula is as follows

$$C_\mu = \frac{1}{A_0 + A_S \frac{U^* K}{\varepsilon}} \tag{5}$$

where $A_0 = 4.04$; $A_S = \sqrt{6}\cos\phi$; ϕ
$$= \frac{1}{3}\arccos(\sqrt{6}W); \quad W$$
$$= \frac{S_{ij}S_{jk}S_{ki}}{\sqrt{S_{ij}S_{ij}}}; \quad S_{ij}$$
$$= \frac{1}{2}\left(\frac{\partial u_i}{\partial x_j} + \frac{\partial u_j}{\partial x_i}\right); \quad U^*$$
$$= \sqrt{S_{ij}S_{ij} + \Omega_{ij}\Omega_{ij}}$$

$2\varepsilon_{ijk}\omega_k$; $\Omega_{ij} = \overline{R_{ij}} - \varepsilon_{ijk}\omega_k$.

The ε equation for the realizable $k−\varepsilon$ model is expressed as

$$\frac{\partial}{\partial t}(\rho\varepsilon) + \frac{\partial}{\partial x_i}(\rho u_i \varepsilon)$$
$$= \frac{\partial}{\partial x_i}\left[\left(\mu + \frac{\mu_t}{\sigma_\varepsilon}\right)\frac{\partial\varepsilon}{\partial x_i}\right] + \rho C_1 S\varepsilon - \rho C_2\frac{\varepsilon^2}{k + \sqrt{\nu\varepsilon}}$$
$$+ C_{1\varepsilon}\frac{\varepsilon}{k}C_{3\varepsilon}G_b + S_k \tag{6}$$

where $C_1 = \max\left(0.43, \frac{\eta}{\eta+5}\right)$; $\eta = \frac{k}{\varepsilon}S$; k is the turbulent kinetic energy, J; $C_{1\varepsilon} = 1.44$; $C_2 = 1.9$; $\sigma_\varepsilon = 1.2$; ε is the turbulent dissipation rate,%; ν is the dynamic viscosity, m²/s;
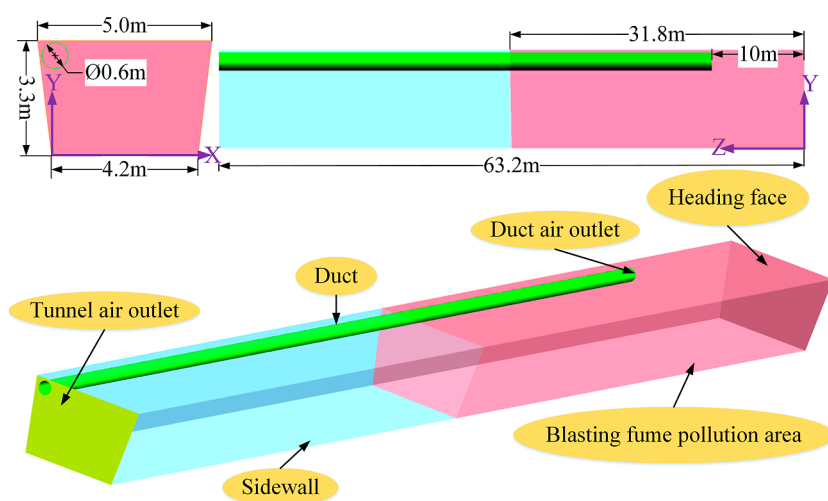
Figure 1. Physical model of the dead-end tunnel.

in this study, the fluid flow is perpendicular to the direction of gravity, hence $C_{3\varepsilon} = 0$.

2.1.5. Component Transport Model. In systems with multiple chemical components, each component must follow the law of conservation of the component mass. The component mass equation is as follows.

$$\frac{\partial(\rho C_S)}{\partial t} + \mathrm{div}(\rho u C_S) = \mathrm{div}(D_S \,\mathrm{grad}\, C_S) + S_S \tag{7}$$

where C_S is the volume concentration of component S; ρC_S is the mass concentration of the component; D_S is the diffusion coefficient of the component; S_S is the production rate of the component.

2.2. Physical Model. The subject of this study is a horizontal dead-end tunnel in an underground phosphate mine, which has a length of 63.2 m. The section is an isosceles trapezoid with a cross-sectional area of 15.18 m². The ventilation duct is installed in the upper-left corner of the roadway, with a diameter of 600 mm and a distance of 10 m from the working face. The exit air velocity is 14 m/s. Figure 1 depicts the full-scale physical model of this tunnel. The origin of the coordinate axes is located at the bottom-left corner of the working face. The X-axis range is (−0.4−4.6), with the positive direction indicating the airflow direction from the duct inlet side to the tunnel return side. The positive direction of the Y-axis is from the tunnel bottom to the tunnel top, within a range of (0−3.3). The positive direction of the Z-axis is from the excavation face to the tunnel exit, covering a range of (0−63.2).

2.3. Mesh Generation and Independence Test. In this study, hexahedral meshes were generated using ICEM software, and an independence test was conducted to select mesh sizes that meet the accuracy requirements.[35] During the meshing process in ICEM, a local refinement was applied to the near-wall regions of the tunnel. The tunnel walls were replaced with stationary no-slip standard walls. The tunnel wall roughness constant was set at 0.5. This study examined three mesh qualities: coarse, medium, and fine, corresponding to mesh sizes of 0.6, 0.4, and 0.2, respectively. The minimum orthogonal quality values were 3.03223×10^{-1}, 2.01234×10^{-1}, and 1.49577×10^{-1}. The number of mesh cells was 158,380, 525,900, and 1,588,615 for the three different mesh sizes, respectively. During the validation process of these three

mesh sizes, a time step of 1 s was used. The sum of the mass flow rates at all inlet and outlet boundaries was less than 1%, meeting the convergence criterion.

Figure 2 shows a comparison of air velocity at the same location in the tunnel for the three different mesh sizes. From
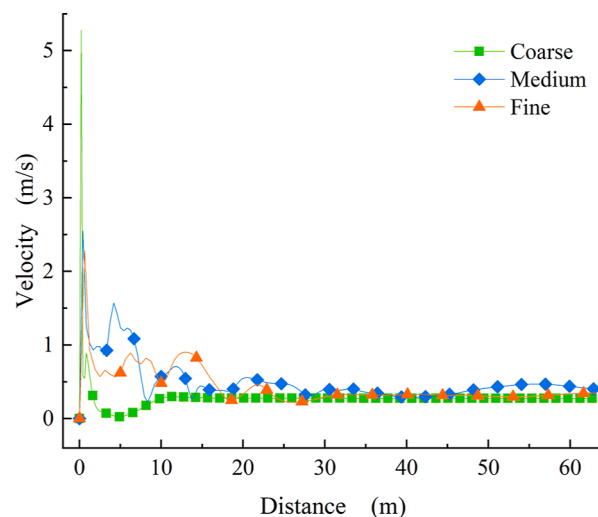

Figure 2. Comparison of air velocities for different mesh sizes.

Figure 2, it can be seen that the air velocity variation trend of the fine mesh is more in line with the variation law of the impinging jet velocity, while the air velocity variation trend of the medium and coarse meshes is poor. Therefore, the fine mesh was selected as the final mesh size, and the mesh quality is shown in Figure 3.

2.4. Parameter Setting. The working face in this study advances 3.4 m per cycle, with a total of 57 blast holes, including 4 large empty holes. The total volume of CO in the roadway is 3.36 m³, and the distance of smoke projection is 31.8 m. The calculation formula for the CO mass fraction in the dispersion area is as follows[36]
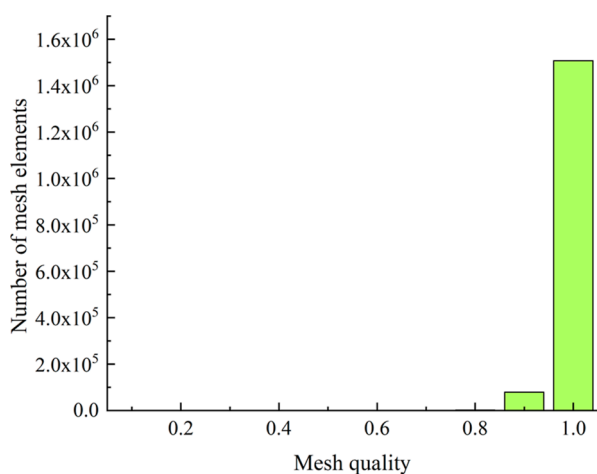
$$C = \frac{Gb}{L_P A} \tag{8}$$

Figure 3. Mesh quality distribution of the fine mesh.

where L_P is the smoke dispersion distance, m; $L_p = 15 + \frac{G}{5}$;[37] G is the explosive mass, kg; b is the CO volume per kg of explosive, m³/kg; and A is the tunnel cross-sectional area, m².

The blast parameters and simulation parameters are shown in Tables 1 and 2, respectively.

Table 1. Blasting Parameter Values

parameter	value
specific charge (q)	1.809 kg/m³
total explosive charge (G)	84 kg
CO volume per kg of explosive (b)	0.04[38]m³/kg
the total volume of CO	3.36 m³

Table 2. FLUENT Boundary Conditions and Parameter Settings

boundary type	boundary definition/value	type	parameter value
inlet1 (velocity inlet)	14 m/s	turbulence model	realizable $k-\varepsilon$ model
outlet	outflow	turbulence intensity (%)	5
wall and duct surface	wall	turbulent viscosity ratio	10
solver type	pressure-based	spatial discretization scheme	second-order upwind
time scheme	transition	pressure-velocity coupling algorithm	SIMPLE

2.5. Model Validation. *2.5.1. Mathematical Model Validation.* Numerous pieces of literature related to mine ventilation numerical simulation have conducted numerical simulation and validation of airflow field. For instance, Kurnia[39] utilized the physical model of Parra[40] to compare and analyze four turbulence models including Spalart-Allmaras, K-Epsilon, K-Omega, and Reynolds Stress Model with the simulated airflow velocity values and corresponding experimental values. Finally, K-Epsilon was found to have the best agreement with the experimental values, with an average error of 30%. Additionally, Whalley and Abdul-Ameer validated the K-Epsilon turbulence model with experimental data from the Parra[40] study, resulting in a R_2 value of 0.96, indicating the applicability of this viscous model for underground mine ventilation numerical simulations.[41]

In this study, the realizable $k-\varepsilon$ model was used, which compared to the $K-\varepsilon$ model, constrains the positive stress C_μ with the strain rate rather than considering it as a constant, thus adding mathematical constraints and ensuring the achievability of the calculation results.[42] Wang used the realizable $k-\varepsilon$ turbulence model to simulate and verify the applicability and accuracy of the airflow field inside the head entry.[12]

2.5.2. Physical Model Validation. To validate the model and related parameters and ensure the practical significance of the simulation scheme in this paper, field tests were conducted. A CO sensor was set up 15 m away from the exit of the head heading, 0.3 m away from the roof, and 2.5 m away from the side wall to monitor the changes in CO values inside the head heading over time, as shown in Figure 4.

Figure 5 shows a comparison between the numerical simulation values at the same monitoring point and the monitoring data of two different periods from those of the CO sensor. It can be seen that the simulation values agree well with the two sets of field monitoring data, with relative errors of 1.69 and 1.78%, respectively. Within the first 7 s of ventilation, the simulation data was close to the monitoring value. During the 8−15 s of ventilation, there was a slight difference between the simulation data and the monitoring data, but the difference was not significant. However, after 23 s of ventilation, there was a significant difference between the simulation data and the monitoring data, which was due to the various factors affecting the exit of the mine, such as wind force, which caused the pressure near the exit to increase and made it difficult to discharge the CO. Overall, the trend of the simulation data was consistent with that of the monitoring data.

3. RESULTS AND DISCUSSION

3.1. Analysis of Airflow and CO Spatiotemporal Evolution under Existing Ventilation Parameters. To understand the airflow and CO distribution in the dead-end tunnel under the existing ventilation parameters, numerical simulations were carried out to study the spatiotemporal evolution of airflow and CO distribution in the entry, which was presented in a visualized way.

3.1.1. Dispersion Characteristics of Airflow in the Dead-End Tunnel. Figures 6 and 7 show the streamlines and velocity cloud map of the airflow in the entry, respectively. As shown in Figure 7, the velocity attenuation rate is very large before the high-speed jet reaches the working face, and the air velocity decreases to 5 m/s when it reaches the working face. The jet impact forms a reverse flow of 3 m/s, but due to the limited space in the entry, part of the jet forms a high-speed vortex ① in front of the working face. Some low-speed reverse flows are entrained into the jet flow continuously at the outlet of the air duct, forming a vortex ②. In addition, due to the pressure difference caused by the jet suction and vortex ②, a range of but weaker vortex ③ is formed near the right wall of the entry. When the jet impacts the working face, an airflow blind zone ④ is formed in the upper-left corner of the entry, where low airflows constantly hover and gradually decrease in velocity. Then, as the distance from the working face increases, the airflow in the entry maintains a direction parallel to the bottom plate and moves slowly toward the exit, and the velocity remains unchanged. The airflow in the entry is in a stable state.

3.1.2. Temporal and Spatial Evolution of CO in the Dead-End Tunnel. Figure 8 presents the CO mass fraction distribution at different times in the ZX section of the dead-
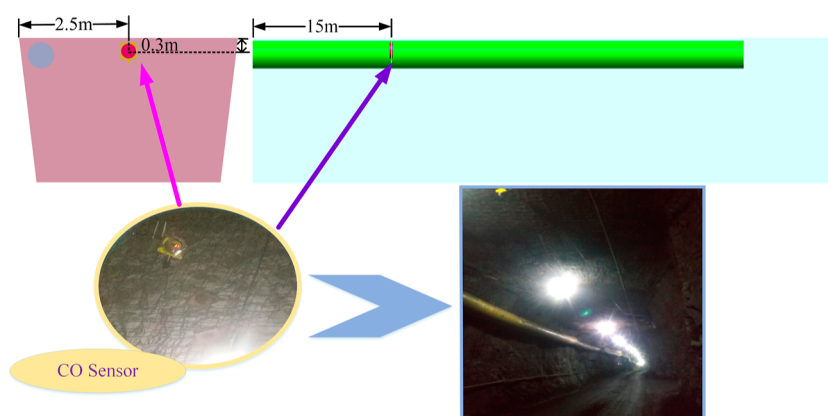
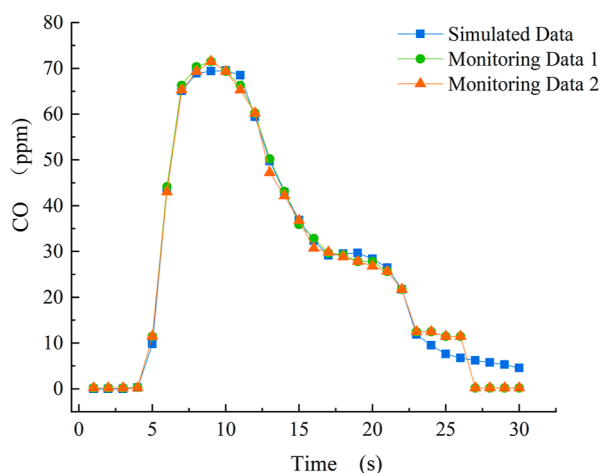**Figure 4.** Actual CO sensor placement in the mine.

Figure 5. Comparison of the numerical simulation and two sets of monitoring data.

end tunnel when $Y = 2.9$ m. In Figure 8a, the CO mass fraction near the face decreases from 6.96×10^{-3} to 6.443×10^{-3} after 5 s of ventilation, and the CO fume starts to move toward the exit due to the entrainment effect of the high-speed jet from the vent. The area closer to the jet has a lower CO mass

fraction. A small CO accumulation area is also observed within the 0.5 m range from the face, and a CO concentration area appears in the blind zone at the upper-left corner of the entry. In Figure 8b, after 50 s of ventilation, the CO fume moves 16 m toward the exit, and the CO mass fraction near the face decreases to 2.148×10^{-3}. The position and mass fraction value of the CO accumulation area in the dead-end tunnel also change accordingly. With the increase in ventilation time, the CO fume in the entry is gradually discharged by the fresh air from the vent. As shown in Figure 8j, when the ventilation time reaches 300 s, the CO in the entry is mostly discharged, and the mass fractions of the CO accumulated near the exit and the two corners also decrease to 1.432×10^{-3} and 2.148×10^{-3}, respectively, which meet the safety threshold according to the Chinese regulation.[43] Therefore, when the ventilation time is 300 s, the CO in the dead-end tunnel drops to a safe level, and the workers can carry out their work safely inside the entry.

Figure 9 shows the CO mass fraction distribution at different times in the Z 0, 10, 20, 30, 40, 50, and 60 m sections of the dead-end tunnel. In Figure 9a, after 10 s of ventilation, the CO near the face in the lower-right corner is first diluted due to the low-speed reverse airflow generated by the jet impacting the face. The airflow, carrying a large amount of CO, moves toward the upper-left corner of the entry due to the entrainment effect of the high-speed jet. In Figure 9d, after
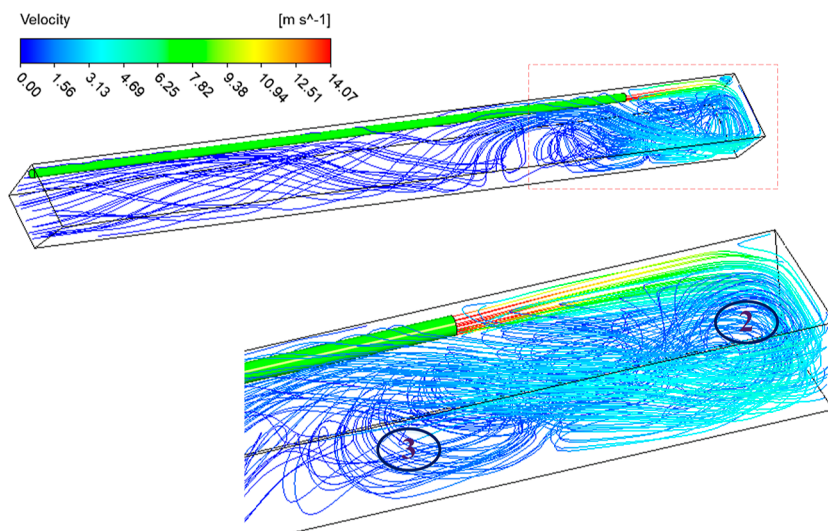

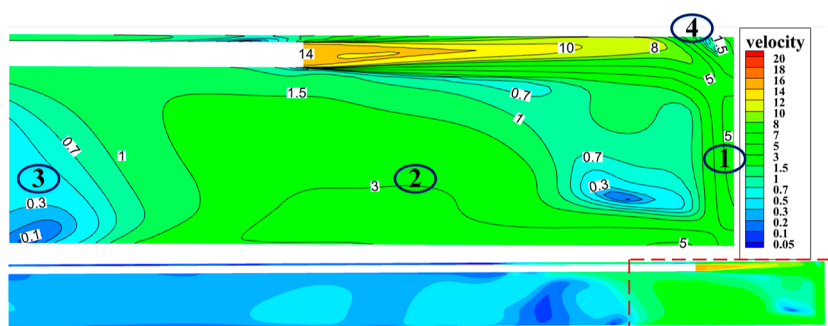**Figure 6.** Streamlines of airflow in the dead-end tunnel.

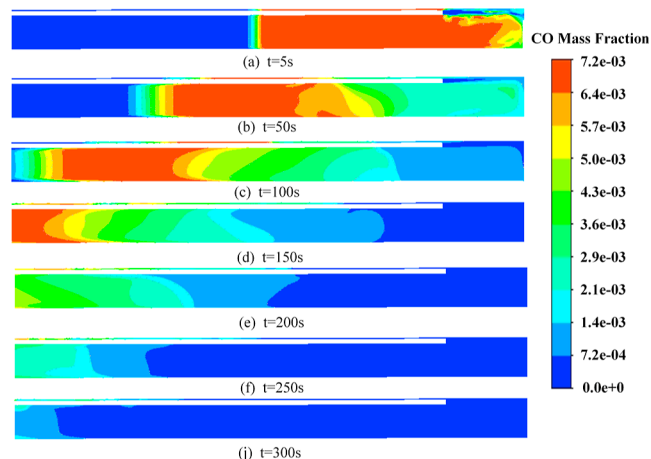**Figure 7.** Velocity cloud map at the exit of the duct in the dead-end tunnel.

Figure 8. CO mass fraction distribution cloud map in the *ZX* section of the dead-end tunnel when *Y* = 2.9 m at different times.

150 s of ventilation, the CO within the 20 m range from the face has been completely discharged, and the fume has diffused to the exit. After 50 s of ventilation, the CO mass fraction near the vent is lower than that in other areas because the reverse airflow, after impacting the left wall of the entry, obtains some kinetic energy, which accelerates the mixing of CO near the vent. When the ventilation time reaches 300 s, the CO mass fraction in the entry drops to $0-2.148 \times 10^{-3}$, which meets the requirement of the Chinese regulation.

3.2. Influence of Different Air Velocities on CO Migration in the Dead-End Tunnel. Increasing the jet velocity can effectively dilute or remove CO in the dead-end tunnel, but as the jet velocity continues to increase, it will have an inhibitory effect on the dilution of CO in the roadway. Therefore, choosing a suitable air velocity at the outlet of the ventilation duct has an important influence on the dilution and removal of CO in the roadway. The "Safety Regulations for Metal and Nonmetal Mines in China" stipulate that the air velocity at the inlet of the underground roadway should not be less than 0.25 m/s. Therefore, when the duct is 10 m away from the working face and 0.5 m away from the tunnel side and the hanging height of the air duct is 2.9 m, air velocities of 14, 16, 18, and 20 m/s are chosen for the dead-end tunnel in this section.

3.2.1. Characteristics of Airflow Dispersion under Different Air Velocities. The airflow field at the *ZX* section *Y* = 2.9 m of the air duct outlet under different air velocities is shown in Figure 10. The analysis shows that as the air velocity increases, the rate of decrease in kinetic energy and air velocity value gradually increases during the movement of the jet toward the

working face. In addition, after the high-speed jet collides with the working face, due to the spatial constraints in the dead-end tunnel and the entrainment effect of the high-speed jet, the positions of eddies ①, ②, and ④ remain almost unchanged and the air velocity values at the edge and center of the eddies increase. The position and intensity of eddy ③ also change continuously with an increase in air velocity. When the duct outlet velocity is 16 m/s, the intensity of the eddy below the air duct increases compared with the roadway under 14 m/s, and the airflow field becomes more chaotic, as shown in Figure 10b. When the air velocity increases to 18 m/s or higher, as shown in Figure 10c,d, the intensity of the eddy below the air duct gradually decreases until it disappears. This is because when the jet velocity reaches a certain value, it causes the low-speed reverse airflow affected by entrainment to be discharged toward the roadway outlet, breaking the source of eddy formation.

To investigate the changes in the CO concentration in the dead-end tunnel under different ventilation schemes, this study selected three central areas (eddies ①, ④, and ③) where CO is prone to accumulating as monitoring points, as shown in Figure 11. The positions of the three monitoring points are point 1 (3.4, 2.9, 2.7), point 2 (−0.14, 2.9, 0.5), and point 3 (4.4, 2.9, 16.2).

3.2.2. Distribution Patterns of CO under Different Air Velocities. Figure 12 shows the variation of the CO mass fraction at the *ZX* cross-section of the dead-end tunnel with different ventilation times and air velocities. When the ventilation time is 5 s, the mass fraction of CO near the excavation face decreases slowly with the increase of the air velocity at the outlet of the duct. When the ventilation time is 100 s, the CO in the tunnel with an air velocity of 14 m/s cannot be exhausted to the tunnel outlet, and the ventilation time needs to be increased to 300 s to reduce the CO mass fraction in the tunnel to meet the requirements of Chinese regulations. When the air velocity reaches 18 and 20 m/s, the high concentration of CO has been exhausted to the tunnel outlet, and the CO concentration in the tunnel has met the requirements of Chinese safety regulations. This is because the increase in air velocity strengthens the dilution and exhaust of CO in the tunnel by carrying the momentum of the jet.

Figure 13 shows the trend of the CO mass fraction at three monitoring points in the tunnel with time. The decreasing rate of CO mass fraction in the tunnel increases with the increase of air velocity, and the trend of air velocity change is more drastic at monitoring point 3 compared to monitoring points 1 and 2. This is because as the air velocity increases, the momentum of the airflow carries more energy to enhance the disturbance at vortex ③. Figure 13a,b, at vortex ② and blind area ④, the initial
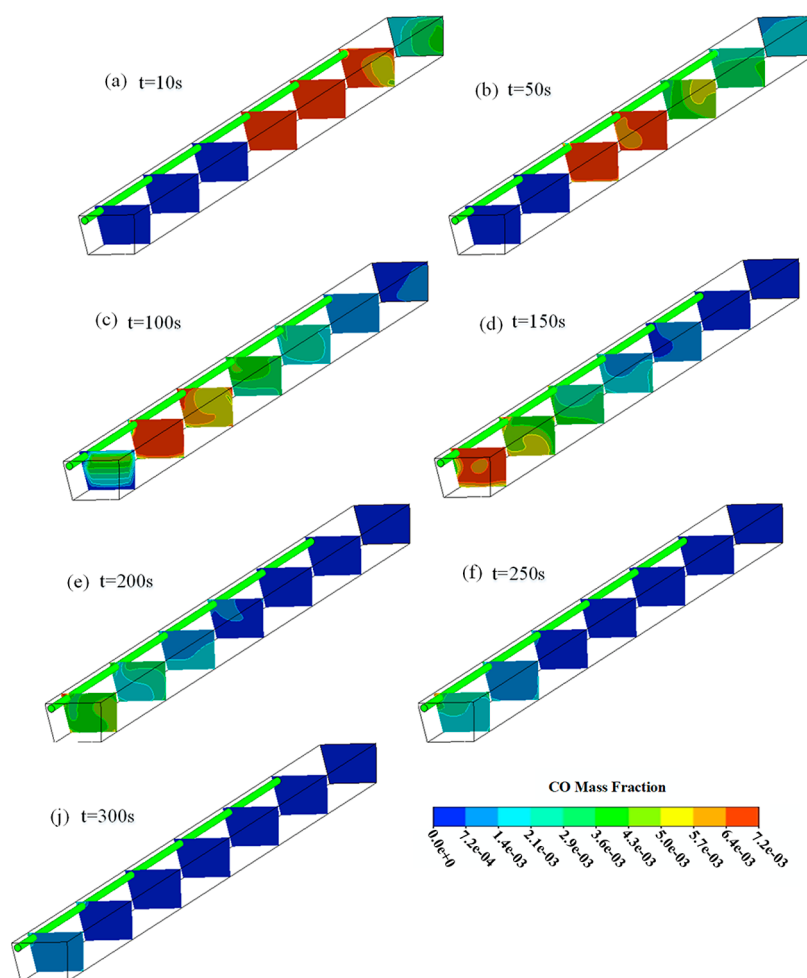
Figure 9. CO mass fraction distribution at different times in the dead-end tunnel.
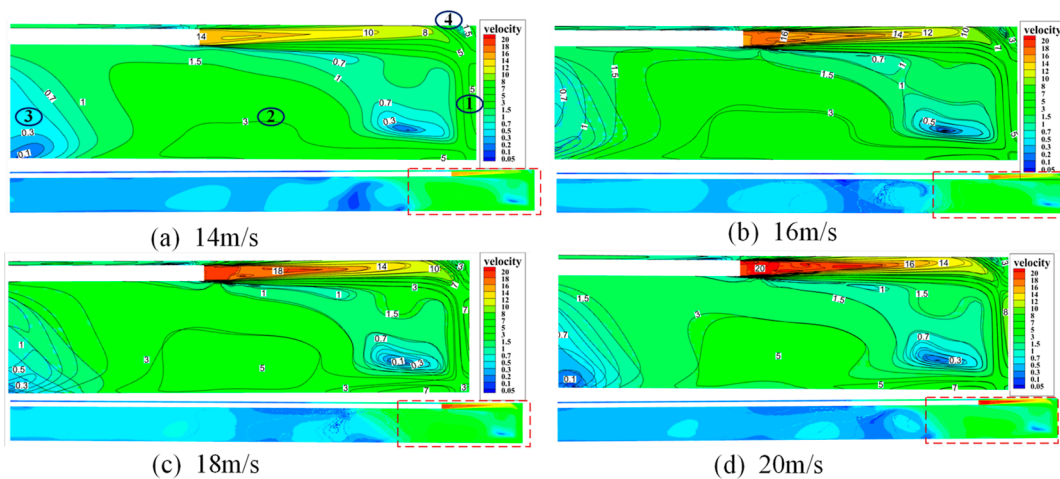

Figure 10. Airflow distribution at *ZX* section *Y* = 2.9 m of the dead-end tunnel under different air velocities.

Figure 11. Location of monitoring points.

mass fraction of CO is highest and the decreasing rate is highest when the air velocity is 16 m/s. At 225 s, the CO mass fraction in the tunnel tends to be zero. In Figure 13c, the trend

of CO mass fraction with time is more chaotic, but the decreasing rate of CO mass fraction is still inversely proportional to the ventilation time after 150 s of ventilation
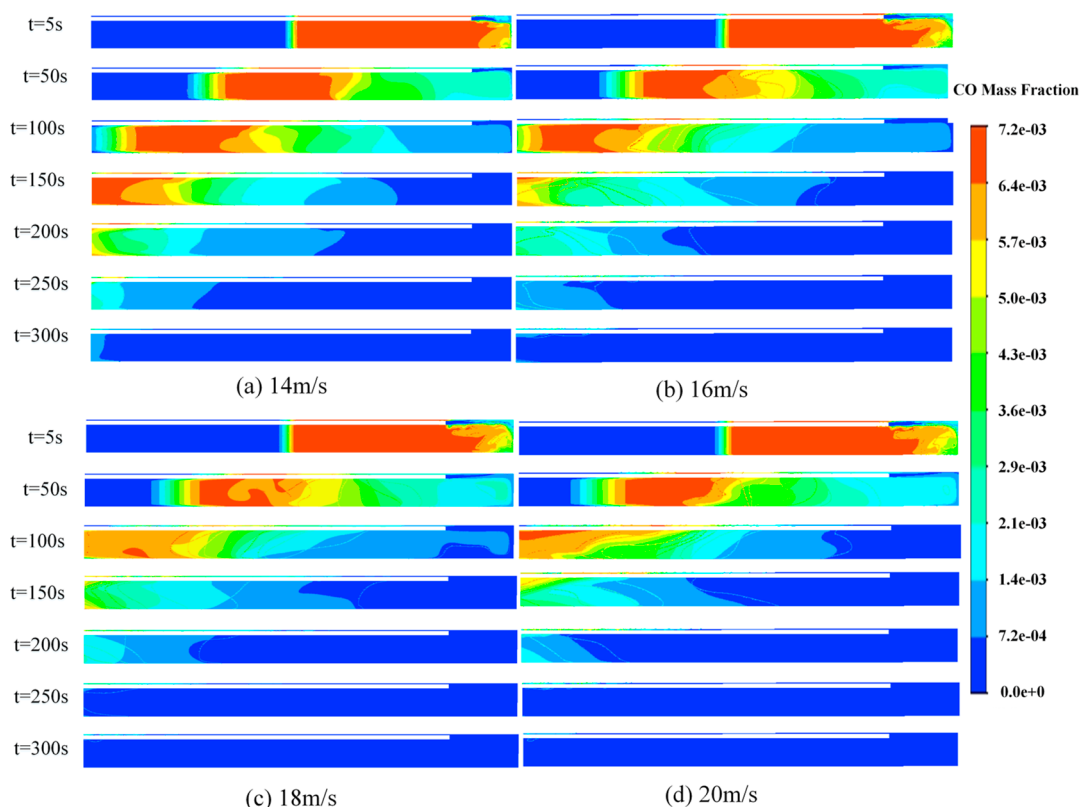
Figure 12. Distribution of the CO mass fraction at different air velocities in the *ZX* section of the 2.9 m *Y*-section dead-end tunnel.
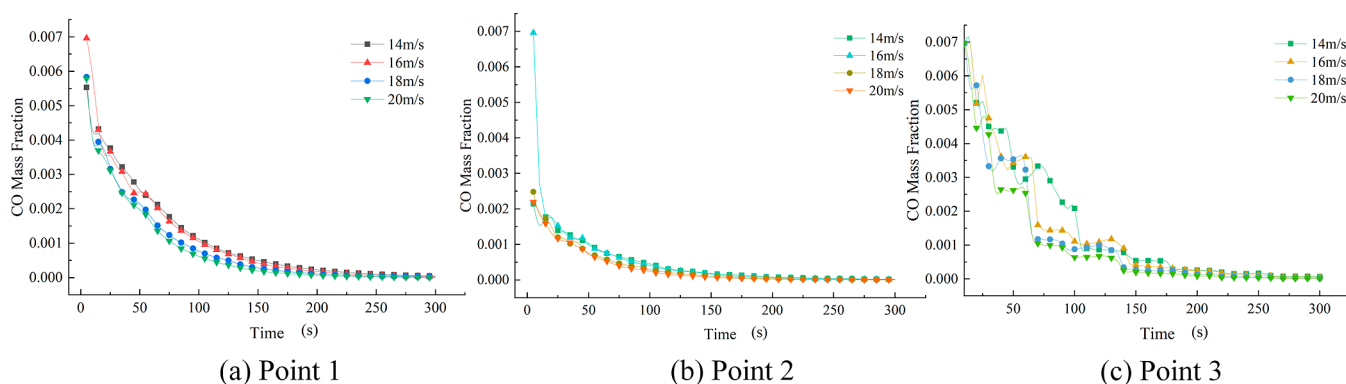

Figure 13. Time evolution of the CO mass fraction at different air velocities in the tunnel.

time. Overall, the CO mass fraction in the tunnel is lowest when the air velocity is 20 m/s.

In conclusion, the air velocity at the outlet of the air duct is inversely proportional to the ventilation time and the CO mass fraction in the tunnel. The air velocity of 20 m/s is more favorable for the dilution and exhaust of CO in the tunnel.

3.3. Impact of Different Distances between the Duct and the Working Face on CO Migration in the Dead-End Tunnel. The distance between the duct and the working face affects whether airflow from the duct outlet can remove the CO at the tunneling working face. Therefore, with a duct air velocity of 14 m/s, a duct-to-wall distance of 0.5 m, and a hanging height of 2.9 m, this section analyzes the impact of four different distances between the duct and the working face (3, 6, 10, and 14 m) on CO migration in the tunneling roadway.

3.3.1. Characteristics of Airflow Diffusion at Different Distances from the Working Face. Figure 14 shows the distribution of the airflow in the *ZX* section of the duct outlet in the tunneling roadway at four different distances. It can be seen from the analysis that the closer the distance between the duct and the working face, the greater the initial kinetic energy of the high-speed jet impacting the working face and the higher the intensity of the vortex ① generated by the reverse airflow being swept by the jet. In addition, as the distance between the duct and the working face increases, the velocity and kinetic energy of the reverse airflow in the roadway decrease, gradually producing almost no suction effect on the surrounding air in the roadway and the shape of vortex ③ gradually disappears. However, the blind zone of the air velocity ④ has not disappeared, and its position remains unchanged. CO easily accumulates in this area and is difficult to remove. Therefore, this study sets a monitoring point (−0.33, 2.9, 0.4) at the
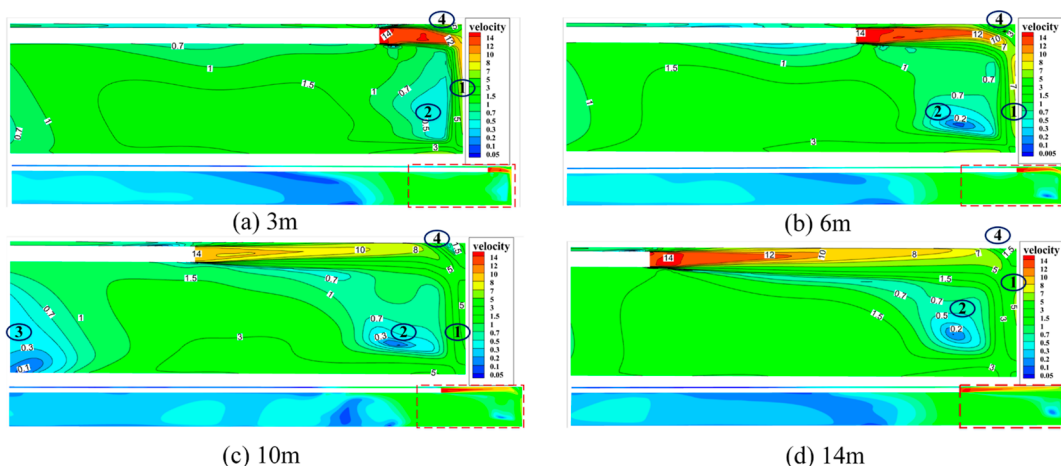
Figure 14. Air velocity distribution cloud map at the duct outlet ZX section at different distances from the working face.
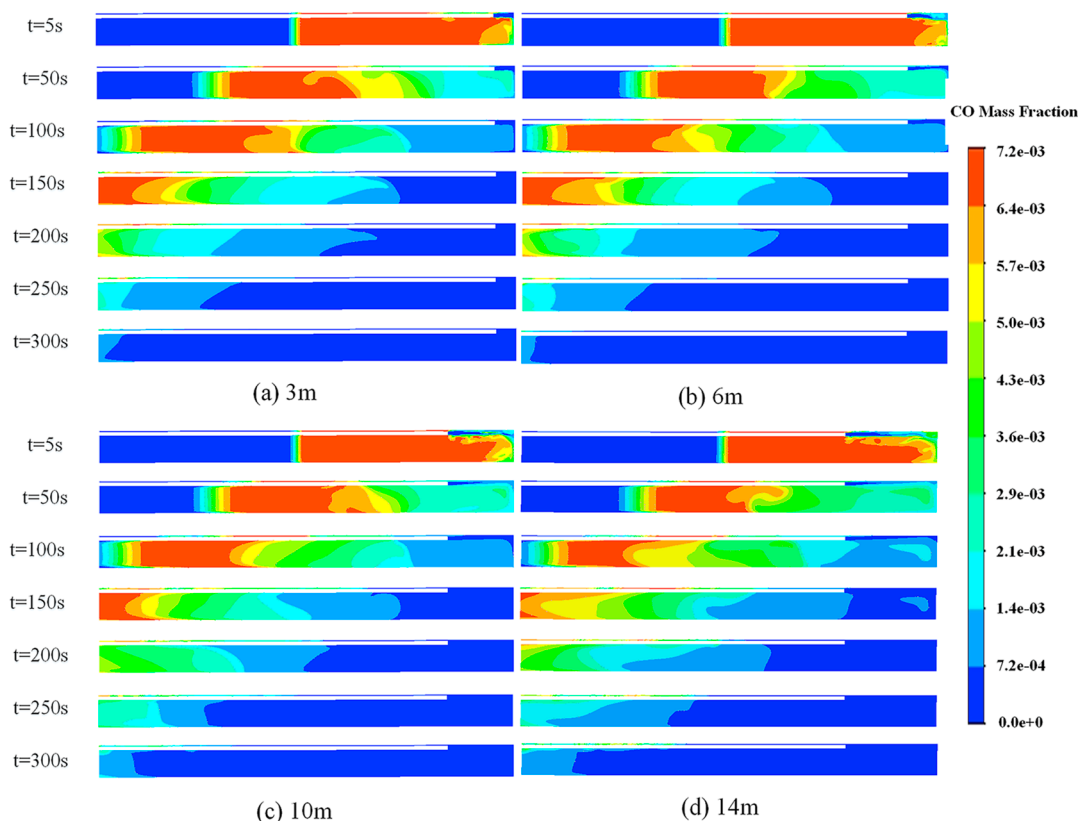

Figure 15. Distribution of CO concentration in the ZX section at Y = 2.9 m in the dead-end at four different distances from the working face.

vortex ④ for comparative analysis of the distribution of CO under different distances between the duct and the working face.

3.3.2. Distribution Patterns of CO at Different Distances from the Working Face. Figure 15 shows the distribution of CO at the $Y = 2.9$ m ZX section in the tunnel at four different distances. Figure 16 illustrates the variation of CO mass fraction along the monitoring line situated 0.1 m from the working face at $t = 5$ s for four distinct distances. The monitoring line extends within the range of (−0.4−4.6, 2.9, 0.1). As the distance between the duct and the working face increases, the velocity and kinetic energy of the reverse airflow generated by the jet impact on the working face decrease, and the mass fraction of CO accumulated near the working face

increases accordingly. As shown in Figure 15a, when the distance between the duct and the working face is 3 m, the CO at the duct outlet and the working face area has been diluted and weakened by $t = 5$ s. In Figure 15b−d, at 5 s, when the distance between the duct and the working face is 6, 10, and 14 m, the mass fraction of CO at the duct outlet and the working face area gradually increases (as shown in Figure 16). In addition, at $t = 5$ s, the farther the distance between the duct and the working face, the stronger the disturbance of air velocity on CO in the range of smoke and debris, and the larger the diffusion range of CO under the duct.

Figure 17 shows the trend of the CO mass fraction at the monitoring point with different distances between the duct and the working face. The monitoring point is situated at
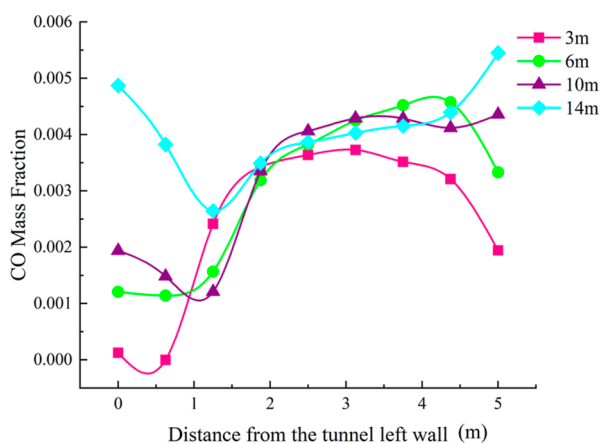
Figure 16. Variation of CO mass fraction near the working face with different distances between the duct and the working face at $t = 5$ s.
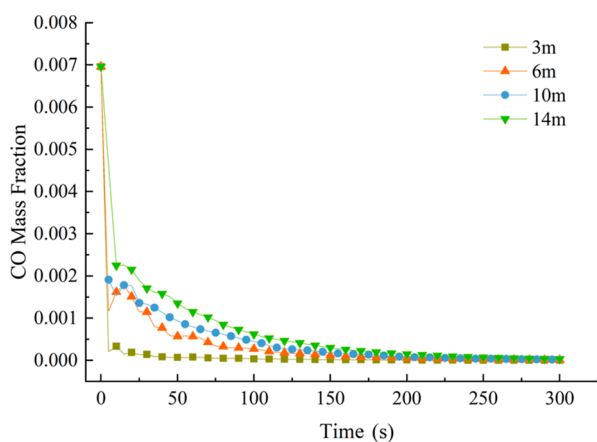

Figure 17. Trend of CO concentration at monitoring point with ventilation time under different distances between the duct and working face.

coordinates (−0.33, 2.9, 0.4), which is at a distance of 9.6 m from the working face. Within 5 s of tunnel ventilation, the CO mass fraction at the monitoring point decreases rapidly and continues to decrease as fresh air flows in. When the distance between the duct and the working face is 3 m, the CO mass fraction at the monitoring point is significantly lower than that of the other three ventilation schemes, and the trend is relatively stable.

In summary, the mass fraction of CO accumulated in the tunnel increases with the distance between the ventilation duct and the working face in the dead-end tunnel. Therefore, when the distance between the ventilation duct and the working face is 3 m, it is more conducive to the discharge of CO in the tunnel.

3.4. Influence of Different Distances between the Duct and Sidewall on CO Migration in the Tunnel. To investigate the influence of different distances between the air duct and the side wall on CO migration in the tunnel, three ventilation schemes were selected in this study: the duct had an air velocity of 14 m/s and was located at 0.5, 1.5, and 2.5 m away from the side wall at a distance of 10 m from the working face and a hanging height of 2.9 m.

3.4.1. Characteristics of Airflow Diffusion at Different Distances from the Sidewall. Figure 18 shows the velocity cloud map of the *ZX* section at *Y* = 2.9 m in a dead-end tunnel

at different distances between the air duct and the side wall. It can be observed that as the distance between the air duct and the side wall increases, the number of eddies on both sides of the duct increases due to the suction of the jet flow at the outlet of the duct. The blind zone③ of the air velocity gradually disappears. As shown in Figure 18c, when the distance between the duct and the side wall is 2.5 m, the space between the duct and the two sides of the tunnel is restricted, and the reverse airflow formed by the high-speed jet flow hitting the working face collides with the two sidewalls, forming a large number of eddies near the side wall.

Region④ is the eddy formed by the airflow colliding with the left wall of the tunnel, and high-concentration CO accumulates there and is difficult to eliminate. To better analyze and compare the three different ventilation schemes, position④ was selected as the monitoring point, with coordinates (−0.28, 2.9, 5.5).

3.4.2. Distribution Patterns of CO at Different Distances from the Sidewall. Figure 19 shows the distribution of CO at different distances between the duct and the side wall at different ventilation times. The analysis indicates that when *t* = 5 s, the CO concentration near the working face increases gradually as the distance between the duct and the side wall increases. When *t* = 50 s, a high concentration CO vortex appears when the distance between the duct and the side wall is 0.5 m, and CO accumulates on the right side of the tunnel due to the presence of more eddies on the right side of the duct, with slower dilution than the left side. With the increase in ventilation time, the position of CO discharge is affected by the airflow, and the dilution rate is also greatly affected. When *t* = 200 s, the CO concentration on the left side of the tunnel is significantly lower than that on the right side when the distance between the duct and the side wall is 2.5 m, as shown in Figure 19c. When *t* = 300 s, the CO in the tunnel with a distance of 0.5 m from the air duct has been discharged, while there is a slightly higher concentration of CO in the dead-end tunnel with a duct distance of 2.5 m that has not been discharged. Generally, the closer the distance between the duct and the side wall, the faster the CO discharge rate.

Figure 20 shows the trend of the CO mass fraction at the monitoring point with ventilation time when the duct is at different distances from the side wall. The monitoring point is positioned at coordinates (−0.28, 2.9, 5.5), which is at a distance of 0.12 m from the left sidewall of the tunnel. The CO mass fraction at the monitoring point is the lowest when the duct is 0.5 m from the side wall, while it is the highest when the duct is 1.5 m from the side wall. This is because there is no influence of eddies when the duct is 0.5 m from the side wall, while there are more eddies with greater intensity at the monitoring point when the duct is 1.5 m from the side wall, which makes CO easier to accumulate, leading to the highest CO mass fraction.

In summary, among the three ventilation schemes above, when the duct is 0.5 m from the side wall, it is more advantageous for CO discharge in the dead-end tunnel.

3.5. Effect of Different Hanging Heights of the Duct on CO Migration in the Dead-End Tunnel. To analyze the effect of different hanging heights of the air duct on CO migration in the heading, this study selected numerical simulation schemes with a duct air velocity of 14 m/s, a distance of 10 m from the working face, 0.5 m from the heading, and 2.9, 1.65, and 0.4 m from the heading floor.
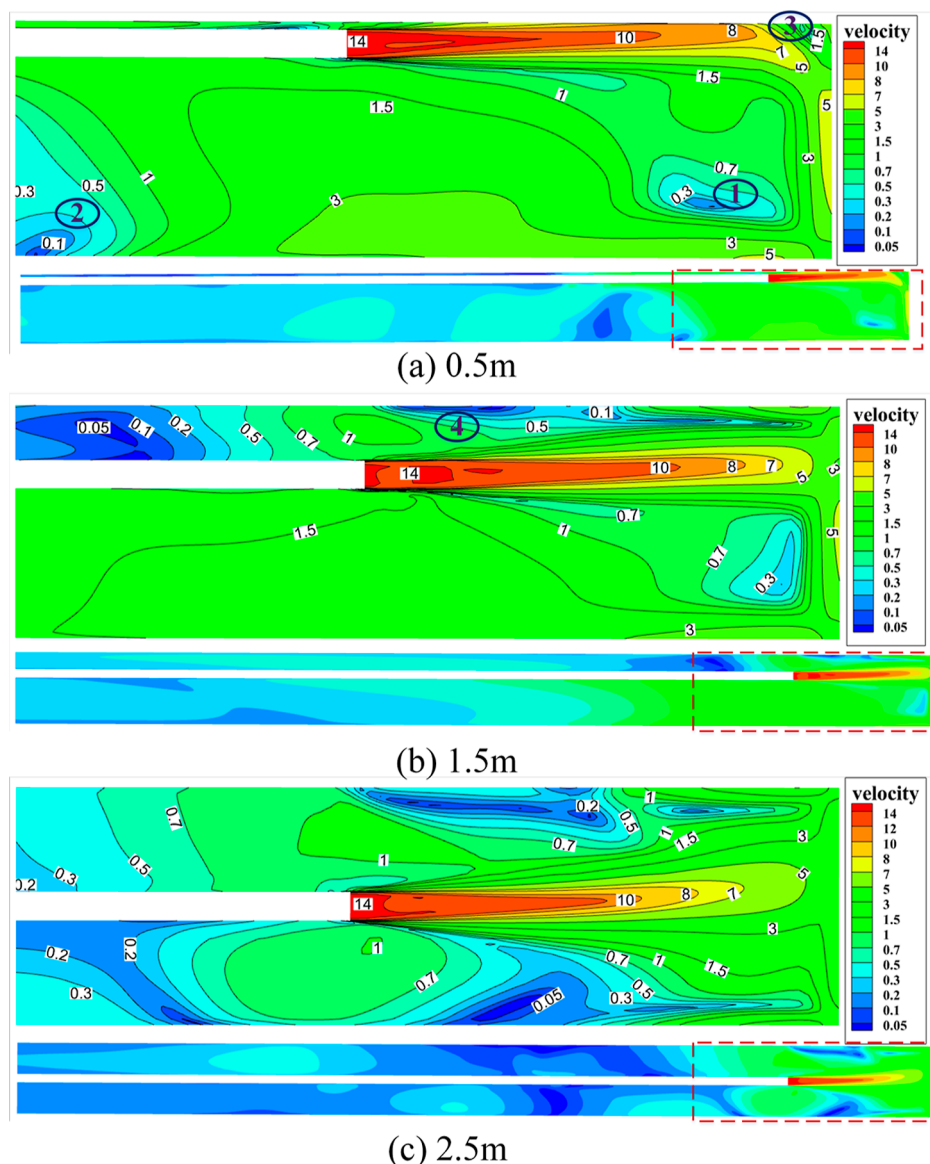
Figure 18. Velocity distribution maps of the *XZ* section at *Y* = 2.9 m in the dead-end tunnel under different distances between the duct and the side wall.
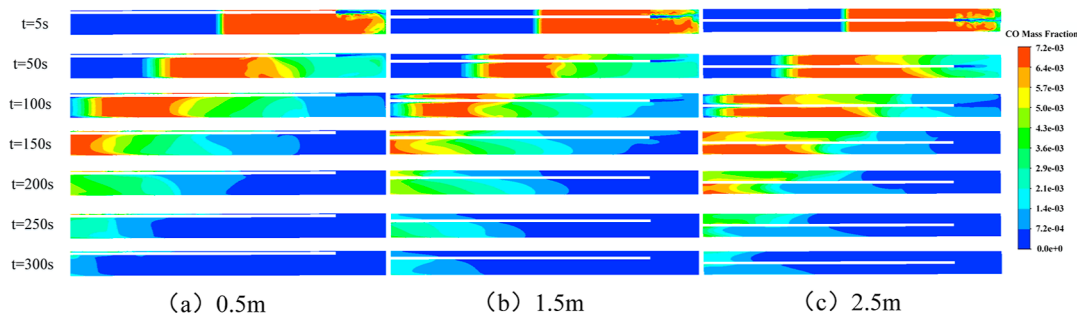

Figure 19. Distribution of the CO concentration at different distances between the duct and the side wall for different ventilation times.

3.5.1. Characteristics of Airflow Diffusion at Different Suspension Heights. Figure 21 shows the airflow cloud map at the *X* = 0.1 m *ZY* section of the heading at different distances from the heading floor. It can be observed that with the decrease of the distance between the duct and the floor, the vortex flow ① in front of the working face experiences three

stages of appearance−disappearance−reappearance; the position of vortex flow ② moves from the floor to the roof of the heading; vortex flow ③ changes from behind the duct to in front of it; and the position of the heading air velocity blind zone ④ changes from the upper-left corner to the lower-right corner. This is because when the duct moves from the roof to
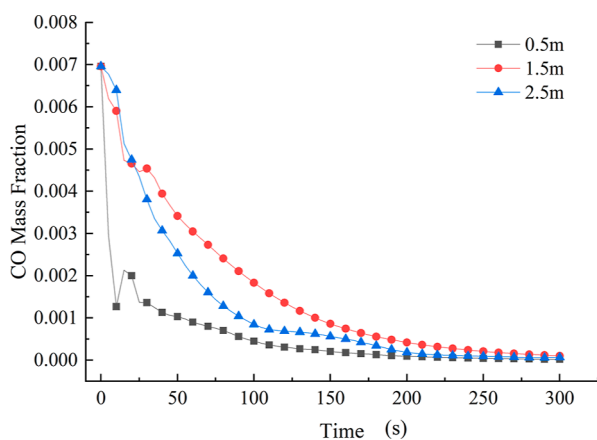
Figure 20. Variation trend of the CO mass fraction at the monitoring point with different distances between the air duct and side wall.

the floor of the heading, the distance between the duct outlet jet and the roof of the heading increases, and the air above the duct is enhanced by the jet's entrainment, leading to an increase in the number and intensity of vortices. In addition, as shown in Figure 21b, when the duct is suspended in the center of the heading, the low-speed reverse airflows on both sides of the duct are affected by the high-speed jet's entrainment, forming a large number of vortices with varying intensities on both sides of the air duct.

However, since the density of CO is less than that of air, CO will gather near the roof of the heading and fresh air will migrate to the floor of the heading under the influence of gravity, making it difficult to eliminate CO. Therefore, this study selected the monitoring point $(-0.3, 2.9, 0.1)$ to analyze the effect of the hanging height of the air duct on the distribution of CO in the heading.

3.5.2. Distribution Patterns of CO at Different Suspension Heights. Figure 22 shows the CO mass fraction distribution in the ZY section of the tunnel at $X = 0.1$ m for different distances
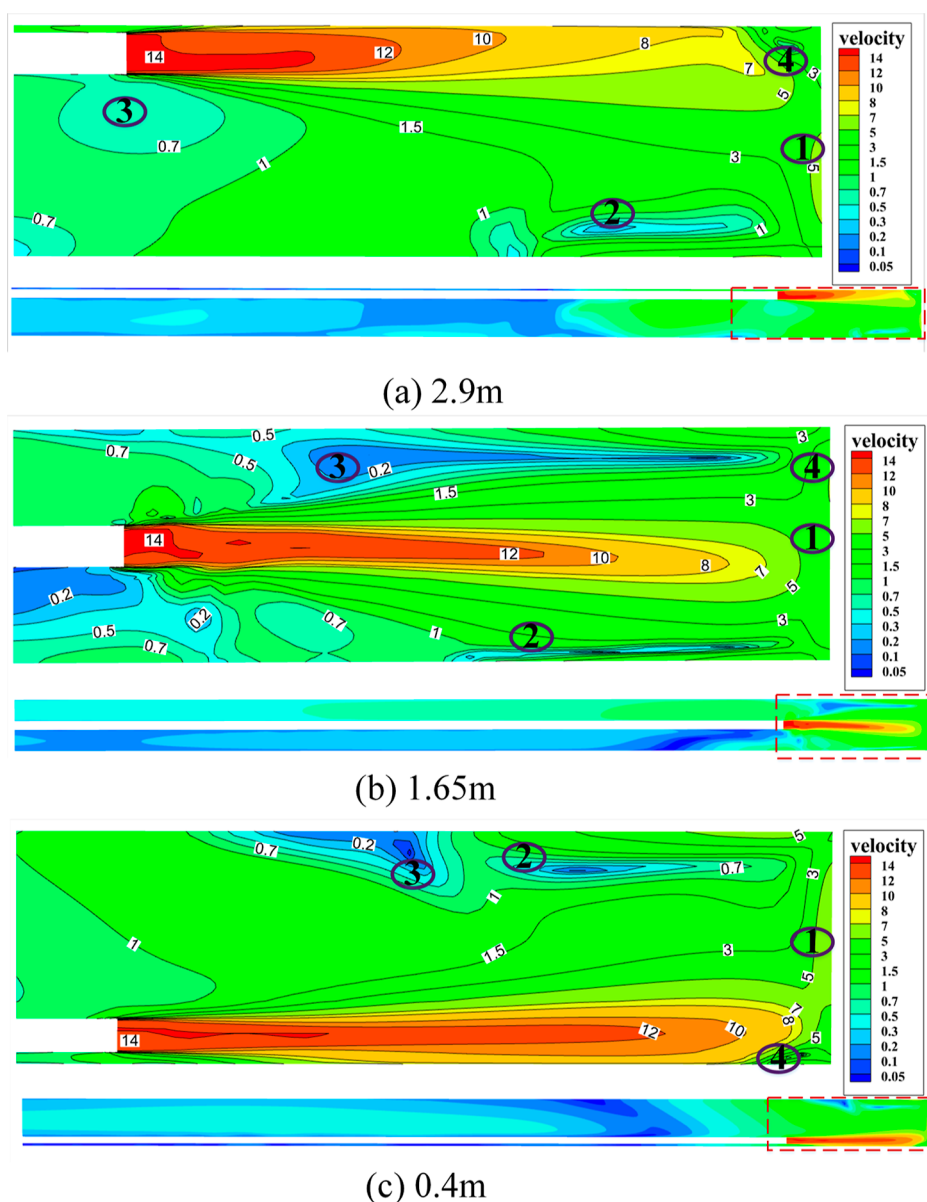

(a) 2.9m

(b) 1.65m

(c) 0.4m

Figure 21. Cloud map of airflow distribution in the ZY section of the roadway at $X = 0.1$ m for different hanging positions of the air duct.
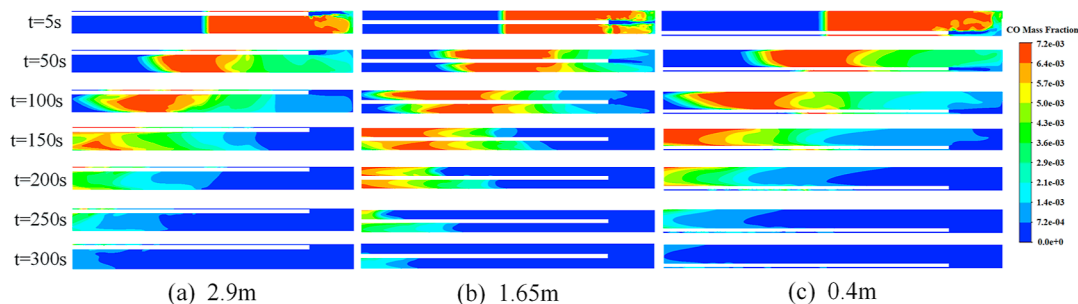
Figure 22. CO concentration distribution in the *ZY* cross-section of the roadway at *X* = 0.1 m at different distances of the duct from the floor.

between the duct and the tunnel bottom. When the ventilation time is 5 s, a large diffusion area of high-concentration CO near the working face can be observed. As shown in Figure 22a,c, from 50 to 100 s of ventilation, the space limitation restricts the jet flow from the duct to expand extensively to both sides of the tunnel, reducing the contact area between the airflow and CO. Therefore, the high-concentration CO accumulation area still exists near the working face. As shown in Figure 22a, fresh air is affected by gravity and migrates toward the tunnel bottom, accelerating the diffusion of CO below the duct. The distance between the duct and the tunnel bottom of 2.9 m is the best ventilation scheme among the three schemes with the highest CO diffusion coefficient and the best ventilation effect.

Figure 23 shows the trend of the CO concentration at the monitoring point with different heights of the duct. The
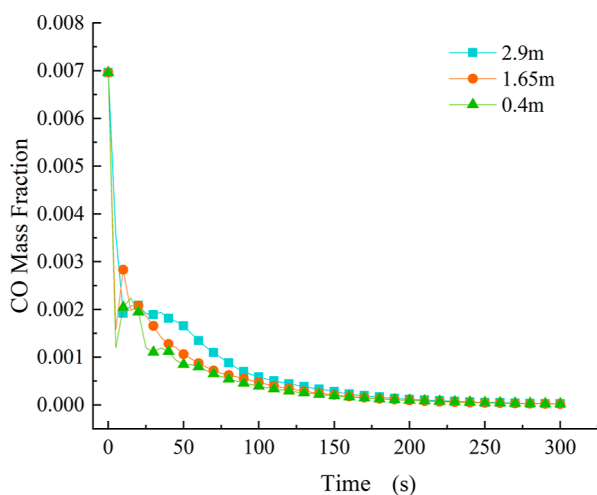

Figure 23. Variation trend of the CO mass fraction at the monitoring point with ventilation time for different suspension positions of the duct.

monitoring point is located at coordinates (0.1, 0.01, 0.02), which is at a distance of 0.02 m from the tunnel floor. The CO mass fraction value at the monitoring point increases inversely proportional to the distance between the duct and the tunnel bottom. Therefore, the distance of 2.9 m between the duct and the tunnel bottom is the best ventilation scheme among the three different schemes.

4. CONCLUSIONS

This study utilizes a component diffusion model to investigate the transport and evolution patterns of airflow and CO concentration within a nonmetallic phosphorite tunnel with an inverted trapezoidal cross-section after excavation blasting. A comparative analysis is conducted on four different ventilation parameters: air velocity at the duct, distance from the duct to the working face, distance from the duct to the sidewall, and duct suspension height. The impacts of these parameters on the airflow field and the CO distribution patterns within the tunnel are analyzed. The main conclusions are as follows:

(1) Under the existing ventilation parameters, vortices form in front of the excavation working face and near the tunnel sidewall's side. Within 5 s of tunnel ventilation, the CO mass fraction near the excavation working face decreases from 6.96×10^{-3} to 6.443×10^{-3}, and after 300 s of ventilation, the CO mass fraction within the tunnel drops below the safety threshold.

(2) Among the different ventilation parameters studied, air velocity has the least effect on the airflow velocity and vortex position in the tunnel, while the distance between the duct and the side wall has the greatest impact. The air velocity near the working face increases with the increase of the duct exit air velocity and the hanging height, while the distance between the duct and the side wall and the hanging height to a certain extent reduces the air velocity near the working face.

(3) Under constant parameters, the CO mass concentration within the tunnel gradually decreases with higher duct outlet velocity and suspension height, showing an inverse proportion to the distance from the duct to the excavation working face and sidewall. Through numerical simulations, it is determined that at an outlet velocity of 20 m/s, a distance of 3 m from the duct to the tunnel entrance, a distance of 0.5 m from the duct to the sidewall, and a suspension height of 2.9 m, the CO mass fraction within the tunnel is minimized. This configuration facilitates rapid dilution and discharge of CO in the tunnel, thereby improving the tunnel's cleanliness during excavation.

Therefore, this research provides a valuable reference and guidance for ventilation design, optimization of ventilation parameters, and mitigation of CO emissions after excavation blasting in inverted trapezoidal tunnels.

■ AUTHOR INFORMATION

Corresponding Author
   Dongping Shi − *School of Environment and Resources, Xiangtan University, Xiangtan 411105, China;* orcid.org/0000-0001-8332-5289; Email: stonextu@163.com

Authors
   Jinmiao Wang − *School of Environment and Resources, Xiangtan University, Xiangtan 411105, China*

Yan Xue − *School of Environment and Resources, Xiangtan University, Xiangtan 411105, China*

Jun Xiao − *School of Environment and Resources, Xiangtan University, Xiangtan 411105, China*

Complete contact information is available at:
https://pubs.acs.org/10.1021/acsomega.3c04819

Author Contributions

Jinmiao Wang: conceptualization, investigation, writing—original draft, writing—review and editing. Yan Xue: methodology, writing—original draft, writing—review and editing, Jun Xiao: writing—review and editing; Dongping Shi: supervision, writing—review and editing.

Notes

The authors declare no competing financial interest.

■ REFERENCES

(1) Wang, J.; Jia, M.; Bin, L.; Wang, L.; Zhong, D. Regulation and Optimization of Air Quantity in a Mine Ventilation Network with Multiple Fans. *Arch. Min. Sci.* **2022**, *67* (1), 179−193.

(2) Shi, D.; Wang, J.; Xiong, L. Study on Noise Correction Algorithm of Infrared Emissivity of Rock under Uniaxial Compression. *Sustainability* **2022**, *14* (19), 12769.

(3) Wencai, W.; Lianjun, D.; Zhihao, Z.; Wei, Z.; Yang, C. The Numerical Simulation of Hanging Position of Local Ventilator in Driving Face. *Min. Saf. Environ. Prot.* **2018**, *45* (6), 15−19 + 24.

(4) Chang, X.; Chai, J.; Luo, J.; Qin, Y.; Xu, Z.; Cao, J. Tunnel Ventilation during Construction and Diffusion of Hazardous Gases Studied by Numerical Simulations. *Build. Environ.* **2020**, *177*, 106902.

(5) Yang, X.; Yu, H.; Wang, Y.; Cheng, W. Investigation of Dust Pollution Control Rules in Tunnel Excavation Based on Modularized Airflow Diverging System. *Build. Environ.* **2022**, *221*, 109356.

(6) De Souza, E. M.; Katsabanis, P. D. On the Prediction of Blasting Toxic Fumes and Dilution Ventilation. *Min. Sci. Technol.* **1991**, *13* (2), 223−235.

(7) Liu, J.; Zhou, H.; Wang, W.; Hu, X.; Ma, Q.; Lu, F. Study of the Diffusion Law of Harmful Gases in Tunnel Construction on Plateaus and Optimization of Ventilation Parameters. *ACS Omega* **2022**, *7* (31), 27135−27148.

(8) Yang, X.; Yu, H.; Wang, Y.; Cheng, W.; Hou, C.; Ye, Y. Study on the Modularized Airflow-Diverging System and Dust-Control Technology in the Fully Mechanized Heading Face. *Powder Technol.* **2022**, *402*, 117325.

(9) Liu, Z.; Gong, X.; Chen, L.; Wei, M.; Cheng, A.; Wu, Y.; Han, Z.; Xue, H.; Niu, H.; Li, H. A Method of Regulating the Wind Field to Reduce Safety Hazards of Gas and Dust in Fully Mechanized Heading Face Based on Dynamic Data. *Heliyon* **2022**, *8* (11), No. e11691.

(10) Zhang, W.; Xue, S.; Tu, Q.; Shi, G.; Zhu, Y. Study on the Distribution Characteristics of Dust with Different Particle Sizes under Forced Ventilation in a Heading Face. *Powder Technol.* **2022**, *406*, 117504.

(11) Obracaj, D.; Korzec, M.; Deszcz, P. Study on Methane Distribution in the Face Zone of the Fully Mechanized Roadway with Overlap Auxiliary Ventilation System. *Energies* **2021**, *14* (19), 6379.

(12) Wang, P.; Gao, R.; Liu, R.; Yang, F. CFD-Based Optimization of the Installation Location of the Wall-Mounted Air Duct in a Fully

Mechanized Excavation Face. *Process Saf. Environ. Prot.* **2020**, *141* (4), 234−245.

(13) Lu, H. Numerical Simulation of the Methane Distribution in Working Face with Auxiliary Ventilation. Master's thesis; Hunan University of Science and Technology: Hunan, 2014.

(14) Zhang, C. Study of Air Flow Field Analysis and Ventilation Optimization in Heading Face Roadway Excavation. Master's thesis; Central South University, 2014.

(15) Wei, N.; Zhongan, J.; Dongmei, T. Numerical Simulation of the Factors Influencing Dust in Drilling Tunnels: Its Application. *Min. Sci. Technol.* **2011**, *21* (1), 11−15.

(16) Xie, Z.; Xiao, Y.; Jiang, C.; Ren, Z.; Li, X.; Yu, K. Numerical Research on Airflow-Dust Migration Behavior and Optimal Forced Air Duct Installation Position in a Subway Tunnel during Drilling Operation. *Powder Technol.* **2021**, *388* (4), 176−191.

(17) Wei, J.; Xu, X.; Jiang, W. Influences of Ventilation Parameters on Flow Field and Dust Migration in an Underground Coal Mine Heading. *Sci. Rep.* **2020**, *10* (1), 8563.

(18) Huang, R.; Shen, X.; Wang, B.; Liao, X. Migration Characteristics of CO under Forced Ventilation after Excavation Roadway Blasting: A Case Study in a Plateau Mine. *J. Cleaner Prod.* **2020**, *267*, 122094.

(19) Zhou, G.; Jing, B.; Xu, Z.; Jiang, B.; Xu, R.; Ren, B.; Sun, B. Simulation Study on Gas-Bearing Dust and Its Application Combined with Air Curtain in Development Heading, a Case Study. *Process Saf. Environ. Prot.* **2022**, *163*, 601−612.

(20) Xin, S.; Wang, W.; Zhang, N.; Zhang, C.; Yuan, S.; Li, H.; Yang, W. Comparative Studies on Control of Thermal Environment in Development Headings Using Force/Exhaust Overlap Ventilation Systems. *J. Build. Eng.* **2021**, *38*, 102227.

(21) Liang, Y.; Lei, B.; Song, S.; Xiao, J.; Kuznetsov, M.; Jordan, T. Numerical Analysis of the Distribution of Combustion Products from Methane Explosions in a Full-Scale Tunnel Using All-Speed CFD Code GASFLOW-MPI. *Energy Sources, Part A* **2023**, *45* (3), 7105−7121.

(22) Mainiero, R. J.; Harris, M. L.; Iii, J. H. R. Dangers of Toxic Fumes from Blasting. *Proceedings of the 33rd Annual Conference on Explosives and Blasting Technique* 2007; pp 1−6.

(23) Li, S.; Zhang, Y.; Ji, H.; Cao, Y. Study on Distribution of CO and Concentration Prediction in Blind Gallery after Blasting Operation. *Arch. Min. Sci.* **2018**, *63* (2), 283.

(24) Chen, J.; Qiu, W.; Rai, P.; Ai, X. Emission Characteristics of CO and NOxfrom Tunnel Blast Design Models:A Comparative Study. *Pol. J. Environ. Stud.* **2021**, *30*, 5503.

(25) Torno, S.; Toraño, J. On the Prediction of Toxic Fumes from Underground Blasting Operations and Dilution Ventilation. Conventional and Numerical Models. *Tunn. Undergr. Space Technol.* **2020**, *96*, 103194.

(26) Zhu, M.; Xie, G.; Liu, L.; Wang, R.; Ruan, S.; Yang, P.; Fang, Z. Strengthening Mechanism of Granulated Blast-Furnace Slag on the Uniaxial Compressive Strength of Modified Magnesium Slag-Based Cemented Backfilling Material. *Process Saf. Environ. Prot.* **2023**, *174*, 722−733.

(27) Liu, C.; Zhang, R.; Wang, Z.; Zhang, X. Research on the Fire Extinguishing Performance of New Gel Foam for Preventing and Controlling the Spontaneous Combustion of Coal Gangue. *Environ. Sci. Pollut. Res.* **2023**, *30* (38), 88548−88562.

(28) Zou, J.; Zhang, R.; Zhou, F.; Zhang, X. Hazardous Area Reconstruction and Law Analysis of Coal Spontaneous Combustion and Gas Coupling Disasters in Goaf Based on DEM-CFD. *ACS Omega* **2023**, *8* (2), 2685−2697.

(29) Torno, S.; Toraño, J.; Ulecia, M.; Allende, C. Conventional and Numerical Models of Blasting Gas Behaviour in Auxiliary Ventilation of Mining Headings. *Tunn. Undergr. Space Technol.* **2013**, *34* (11), 73−81.

(30) Ding, H.; Quan, M.; Shi, X.; Xu, Y.; Deng, Q.; Liu, K. Study on Numerical Simulation of Blasting Fume Migration Laws in Tunnel with Drilling and Blasting Construction. *J. Saf. Sci. Technol.* **2020**, *16* (04), 82−87.

(31) Ting, D. S.-K. Chapter 2—Equations of Fluid in Motion. In *Basics of Engineering Turbulence*; Ting, D. S.-K., Ed.; Academic Press, 2016; pp 19−46.

(32) Wang, X. Research on Distribution of Carbon Monoxide from Blasting Smoke in Single-Heading Tunnel and Optimization of Arrangement of Air Ducts. Master's thesis; Kunming University of Science and Technology: Yunnan, 2021.

(33) Shiau, J.; Al-Asadi, F. Determination of Critical Tunnel Heading Pressures Using Stability Factors. *Comput. Geotech.* **2020**, *119*, 103345.

(34) Chao, L.; Yanbo, S.; Yangge, Z.; Kehua, L.; Guang, Y. Overview of Flow Field Characteristics of Reactor for Beneficiation Reagent Production Based on CFD Technology. *Conserv. Util. Miner. Resour.* **2019**, *39* (5), 135.

(35) Li, B.; Hu, H.; Long, Y.; Zhan, S.; Zhang, Z.; Li, W.; Li, J.; Gong, J. Dust Transport Behaviour in the Nanwenhe Extra-Large Stepped Underground Metal Mine Stope. *J. Cleaner Prod.* **2022**, *372*, 133699.

(36) Wei, N.; Li, L.; Wang, C. Analysis of Harmful Gas Concentrations Variation in Tunneling Ventilation. *J. China Three Gorges Univ., Nat. Sci.* **2006**, *28* (04), 324−327.

(37) Yong-jun, Y.; Jun-ting, J.; De-xin, D.; Yong-ming, Z.; Chao, X. Transport of Radon and Blasting-Fume in Blind Roadway with Exhaust Ventilation after Blasting. *China Saf. Sci. J.* **2015**, *25* (5), 131−137.

(38) Ma, D.; Zou, C.; Li, Z.; Zhang, S.; An, Y. Numerical Simulation on Optimization of Blasting Smoke Ventilation Parameters in Blind Roadway Based on CFD. *Value Eng.* **2023**, *42* (17), 103−107.

(39) Kurnia, J. C.; Sasmito, A. P.; Mujumdar, A. S. CFD Simulation of Methane Dispersion and Innovative Methane Management in Underground Mining Faces. *Appl. Math. Model* **2014**, *38* (14), 3467−3484.

(40) Parra, M. T.; Villafruela, J. M.; Castro, F.; Méndez, C. Numerical and Experimental Analysis of Different Ventilation Systems in Deep Mines. *Build. Environ.* **2006**, *41* (2), 87−93.

(41) Whalley, R.; Abdul-Ameer, A. The Dynamics of Cyclic Ventilation Systems. *Appl. Math. Model* **2011**, *35* (1), 93−108.

(42) Launder, B. E.; Spalding, D. B. The Numerical Computation of Turbulent Flows. *Comput. Methods Appl. Mech. Eng.* **1974**, *3* (2), 269−289.

(43) *Safety Regulations for Metal and Nonmetal Mines*, GB16423-2020; Beijing, 2020.